Chemical Science

ROYAL SOCIETY OF CHEMISTRY

EDGE ARTICLE

Published on 11 November 2026
Licensed under CC-BY-NC 4.0

Check for updates

Cite this: DOI: 10.1039/d6sc07112k

Coordination-gated oxovanadium electrolyte for scalable high-temperature vanadium flow batteries

Haoyang Long,†[abc] Zheyu Zhao,†[d] Tao Liu,[ac] Feng Xing,[a] Jichun Jiang,[e] Lei Hua,[e] Shengli Chen,[df] Congxin Xie*[acf] and Xianfeng Li*[ac]

Received 17th September 2026
Accepted 22nd October 2026

DOI: 10.1039/d6sc07112k

rsc.li/chemical-science

Vanadium flow batteries (VFBs) are promising for grid-scale energy storage, but their thermal operating window is limited by VO_2^+ instability. Above 45 °C, VO_2^+ undergoes oxo-bridged condensation and causes V_2O_5 precipitation, leading to system failure. Here we report a heterocationic coordination-gating strategy to regulate V(v) condensation. In the designed electrolyte, Ti(iv) exists as TiO^{2+}-like oxophilic units that form VO_2^+ through persistent V–O–Ti bridges. These bridges occupy reactive oxo sites of V(v) species, gating V–O–V network formation and delaying V_2O_5 nucleation. Consequently, a 2 M VO_2^+ electrolyte containing TiO^{2+} remains stable for 40 days at 50 °C (*vs.* 12 h for pristine 2 M VO_2^+ electrolyte). A VFB with this electrolyte maintains stable cycling for over 2000 cycles at 50 °C. Moreover, a 10 kW VFB stack operates stably for nearly 500 cycles at approximately 50 °C, demonstrating its practical feasibility. Experimental studies and economic analysis support that the cation–VO_2^+ oxygen-bridged coordination strategy is universal and efficient.

Introduction

Long duration energy storage (LDES) technologies are critical for integrating a large portion of intermittent renewables into grids.[1] Among available technologies, vanadium flow batteries (VFBs) are well suitable for LDES due to their features of decoupled power and energy, high safety and long cycle life. Nevertheless, their practical deployment is still constrained by the positive electrolyte, where VO_2^+ can convert to V_2O_5 at a high state of charge and temperatures above 45 °C[2] (Fig. 1a). The precipitate not only causes capacity decay and efficiency loss, but can also block the pump and flow channels, induce severe stack polarization, and ultimately lead to system failure. Therefore, VFB systems must rely on active thermal management to ensure their reliability.

For the precipitation process of vanadium (V), the transformation of $[VO_2(H_2O)_3]^+$ to V_2O_5 is widely accepted to occur *via* a two-step reaction process (eqn (1)–(3)), in which $VO(OH)_3$ serves as an intermediate species formed through deprotonation.[3–8] Our recent study demonstrated that $[VO_2(H_2O)_3]^+$ undergoes water dissociation and stepwise deprotonation to form the hydroxylated intermediate $VO(OH)_3$, with the second deprotonation identified as the rate-determining step.[7] Subsequently, adjacent $VO(OH)_3$ units condense through dehydration, generating V–O–V-bridged oligomers and polynuclear vanadium oxide networks that ultimately lead to V_2O_5 precipitation.[9] During the process, V–O–V bond formation is essential for the precipitation. Accordingly, a rational stabilization strategy can directly target the subsequent V–O–V condensation step rather than merely shifting the hydrolysis equilibrium.

$$[VO_2(H_2O)_3]^+ \rightarrow VO(OH)_3 + H_3O^+ \quad (1)$$

$$2VO(OH)_3 \rightarrow V_2O_5 + 3H_2O \quad (2)$$

$$2VO_2^+ + H_2O \rightarrow V_2O_5 + 2H^+ \quad (3)$$

A heterocationic coordination interaction can be leveraged. We try to occupy the reactive oxygen sites of VO_2^+ *via* a foreign cation center through V–O–M bridges, and the formation of V–O–V linkages can be kinetically avoided. Although VO_2^+ is formally cationic, its V–O bonds are strongly polarized, leaving the terminal oxygen atoms with appreciable lone-pair electron density and hard-base character. Upon encountering a high-charge-density, strongly oxophilic hard Lewis acid, these terminal oxo ligands can be converted into bridging oxo motifs, giving rise to robust heterocationic V–O–M oxygen bridges.[10]

[a]Division of Energy Storage, Dalian National Laboratory for Clean Energy, Dalian Institute of Chemical Physics, Chinese Academy of Sciences, 457 Zhongshan Road, Dalian 116023, China. E-mail: xiecongxin@dicp.ac.cn; lixianfeng@dicp.ac.cn

[b]School of Chemistry and Chemical Engineering, University of Chinese Academy of Sciences, Beijing 100049, China

[c]Key Laboratory of Long-Duration and Large-Scale Energy Storage, Chinese Academy of Sciences, China

[d]Hubei Key Laboratory of Electrochemical Power Sources, College of Chemistry and Molecular Sciences, Wuhan University, Wuhan 430072, China

[e]Liaoning Key Laboratory for Mass Spectrometry Technology and Instrumentation, Dalian Institute of Chemical Physics, Chinese Academy of Sciences, Dalian 116023, China

[f]Liaoning Binhai Laboratory, Dalian 116023, China

† These authors contributed equally to this work.

© 2026 The Author(s). Published by the Royal Society of Chemistry

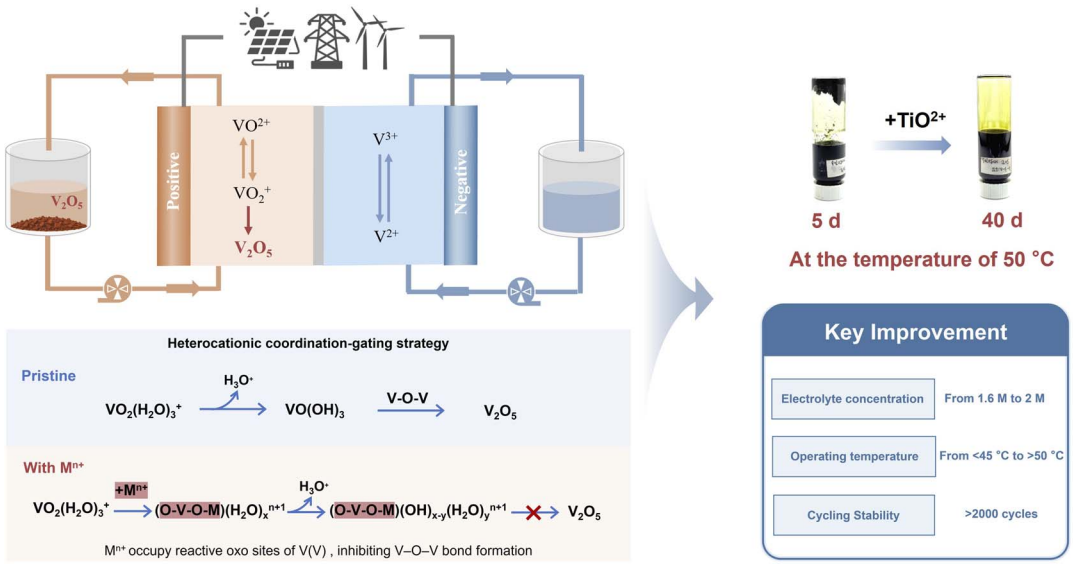


Fig. 1 Schematic diagram of precipitation process regulation by the cation stabilizer and enhanced VFB performance. In VFBs, VO_2^+ in the positive electrolyte can precipitate as V_2O_5 at temperatures above 45 °C. The cation stabilizer as a coordination gate can inhibit V–O–V bond formation and suppress the precipitation reaction, thereby enabling higher vanadium concentrations, a wider operating-temperature range, and improved cycling stability.

Such oxygen-bridged cation–cation interactions are well known in actinyl[11–14] and vanadyl[15,16] chemistry, where oxo ligands of AnO_2^+ or VO_2^+ can bridge to other metal centers. In a concentrated battery electrolyte, such interactions can be regarded as dynamic heterocationic coordination nodes embedded within the solvation network, thereby inhibiting the condensation of vanadium species.

Here, we propose a universal heterocationic coordination-gating strategy. Ti(IV) is introduced as an oxophilic coordination node to prove the concept. Under strongly acidic sulfate conditions, Ti(IV) exists predominantly as titanyl-like TiO^{2+} species.[17] Its d^0 electronic configuration and hard-Lewis-acid character render Ti(IV) capable of forming heterocationic V–O–Ti oxygen bridges with vanadium (V). We demonstrate that TiO^{2+} couples with VO_2^+ to generate thermally persistent VO_2^+–TiO^{2+} oxygen-bridged complexes through V–O–Ti oxygen bridges by MS, XAS and computational simulations. TiO^{2+} acts as local coordination gates to suppress the conversion of isolated V(V) species into V–O–V aggregates. As a result, the vanadium concentration on the positive side can be increased from 1.6 to 2 mol L^{-1}, and the pentavalent electrolyte remains stable for 40 days at 50 °C. A single VFB assembled with this coordination-regulated electrolyte cycles for more than 2000 cycles at 50 °C without precipitation, while a 10 kW VFB stack operates stably for nearly 500 cycles within 47∼52 °C. Moreover, Ti-containing electrolyte reduces VFB system cost effectively, confirming its practical feasibility and economic advantage for large-scale application. Spectroscopic studies and theoretical calculations further reveal that TiO^{2+}, VO^{2+}, Cr^{3+}, and Fe^{3+} can form stable oxygen-bridged interactions with VO_2^+ and markedly enhance V(V) electrolyte stability. These results establish cation–VO_2^+ coordination as a molecular-level design principle for high-temperature-stable vanadium electrolytes.

Results and discussion

The role of V–O–V formation and the design rationale in high-temperature-stable electrolytes

To clarify the role of V–O–V in V(V) precipitation, we performed *in situ* Raman measurements on a 2 M VO_2^+ electrolyte at different temperatures (Fig. S1, SI). The SO_4^{2-} symmetric-stretching[18] band at 985 cm^{-1} decreased as temperature increased from 25 to 60 °C. This change can be attributed to H_2SO_4 association[19] and release associated with deprotonation of $[VO_2(H_2O)_3]^+$, which together shifts sulfate speciation from SO_4^{2-} toward HSO_4^- and H_2SO_4 (Fig. S2, SI). We then monitored V_2O_5 formation by rapid, continuous Raman acquisition at 50 °C. As shown in Fig. 2a, the initial electrolyte mainly contained solvated $[VO_2(H_2O)_3]^+$ and $VO(OH)_3$, whereas characteristic V_2O_5 bands[20] appeared at the final stage, confirming precipitate formation. During the intermediate stage, two bands at 485 and 805 cm^{-1} emerged, gradually intensified, and red-shifted with heating time, while the VO_2^+ symmetric-stretching signal (∼935 cm^{-1}) weakened. Before precipitation, the overall Raman intensity quickly decreased, and the bands shifted to 469 and 778 cm^{-1} became dominant. According to previous reports, the bands at approximately 485 and 805 cm^{-1} correspond to V–O bridge vibration and V–O–V stretching, respectively.[16,21] These observations indicate that V(V) species condense through V–O–V linkages at elevated temperature. A hydroxyl oxygen of one $VO(OH)_3$ unit can attack the V center of a neighboring unit to form a V–O–V bridge through an SN2-type dehydration–transformation pathway.[9] The red shift likely reflects restricted V–O–V vibration as the degree of aggregation increases. The initially formed dimers undergo successive dehydration and condensation reactions, progressively generating larger vanadium-oxide clusters.[9] Once aggregates reach

© 2026 The Author(s). Published by the Royal Society of Chemistry

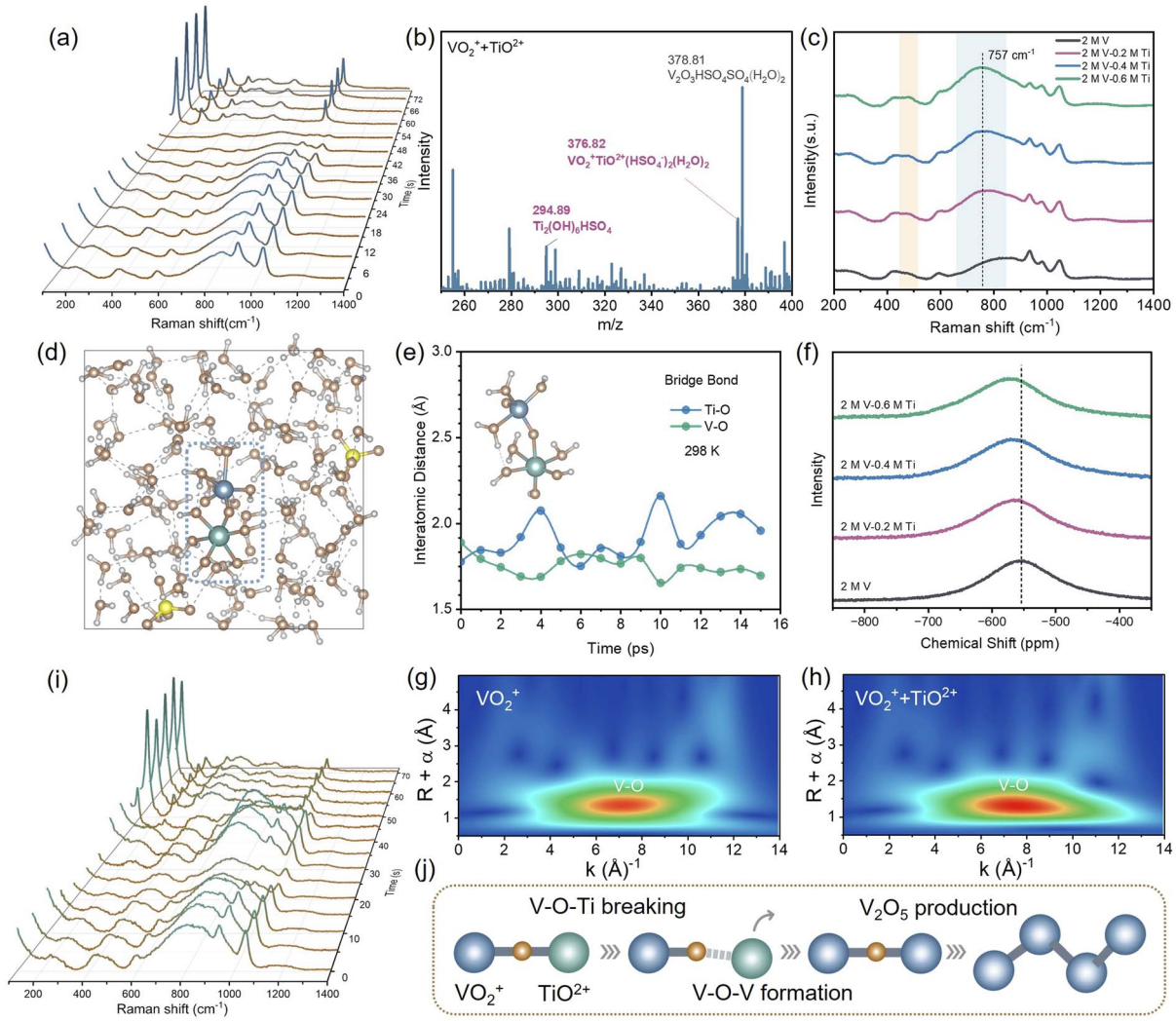


Fig. 2 Design of a high-temperature-stable electrolyte. (a) *In situ* Raman spectra of the V(v) precipitation process for 2 M VO_2^+ electrolyte at 50 °C. (b) MS spectrum of a diluted sample prepared from electrolyte containing 1.5 M VO_2^+ and 0.6 M TiO^{2+}. (c) Raman spectra of 2 M VO_2^+ electrolytes with different TiO^{2+} concentrations. (d) Representative AIMD configuration of the VO_2^+–TiO^{2+} system in aqueous electrolyte at 298 K. (e) Time evolution of V–O and Ti–O interatomic distances in the V–O–Ti bridge of the VO_2^+–TiO^{2+} structure shown in the inset at 298 K. (f) ^{51}V NMR spectra of 2 M VO_2^+ electrolytes with different TiO^{2+} concentrations. Wavelet transforms of V K-edge EXAFS for (g) 1.5 M VO_2^+ solution and (h) 1.5 M VO_2^+ solution with 0.6 M TiO^{2+}. (i) *In situ* Raman spectra of the V(v) precipitation process for 2 M VO_2^+ electrolyte with 0.6 M TiO^{2+} at 80 °C. (j) Proposed precipitation pathway after TiO^{2+} introduction.

a critical size, solid V_2O_5 forms. Thus, *in situ* Raman spectroscopy further identifies V–O–V bond formation as a key precursor step in V(v) precipitation.

We therefore sought to interrupt the V–O–V formation step by adding a cation that can form heterocationic V–O–M (M = cation) oxygen bridges with VO_2^+. Here, Ti(IV) was selected because it is a common d^0 cation and demonstrates hard-Lewis-acid character. Ti(IV) is also known to undergo self-polymerization[22] and to interact with other cations,[23] suggesting that TiO^{2+} can coordinate with VO_2^+. To probe the heterocationic motifs of TiO^{2+} and VO_2^+, time-of-flight mass spectrometry (MS) was performed using pneumatic nebulization (Fig. S3, SI), which reduces damage to solution-phase complexes. For the pristine VO_2^+ electrolyte, $[VO_2(H_2O)_3]^+$ was detected as the dominant species (Fig. S4, SI), consistent with the accepted V(v) solvation structure.[24,25] After TiO^{2+} addition, a VO_2^+–TiO^{2+} complex appeared at $m/z = 376.82$ (Fig. 2b), and its experimental isotopic pattern was in good agreement with the theoretical isotopic distribution (Fig. S5, SI). It should be noted that, because MS was conducted under diluted solution conditions, the detected species may not fully represent those present in the original concentrated electrolyte. VO_2^+–TiO^{2+} complexes were therefore further evaluated using Raman, ^{51}V-NMR, and XAS measurements at the original electrolyte concentration.

In the Raman spectra, as TiO^{2+} concentration increased, bands at 476 and 757 cm^{-1} appeared and intensified (Fig. 2c), matching reported V–O–M vibrations.[14–16] AIMD simulations of VO_2^+, TiO^{2+}, and mixed VO_2^+/TiO^{2+} systems (Fig. 2d, S6 and S7, SI) showed that an oxygen-bridged VO_2^+–TiO^{2+} motif remained intact in the mixed VO_2^+/TiO^{2+} system during the simulated

© 2026 The Author(s). Published by the Royal Society of Chemistry

timescale (Fig. 2d). At both 298 K and 323 K, the V–O and Ti–O distances in the V–O–Ti bridge exhibited thermal fluctuations without sustained bond elongation leading to dissociation (Fig. 2e, S8 and S9, SI). Constrained molecular dynamics calculations revealed substantial free-energy increases upon stretching the bridging V–O and Ti–O bonds (Fig. S10, SI). These results supported the structural persistence and resistance to dissociation of the V–O–Ti bridge under the investigated conditions. In ^{51}V NMR spectra (Fig. 2f), the V(v) resonance shifted upfield with increasing TiO^{2+} content, implying enhanced electronic shielding. Calculated shielding factors were also higher for V(v) in the VO_2^+–TiO^{2+} complexes than in solvated VO_2^+ (Fig. S11, SI), supporting the formation of oxygen-bridged VO_2^+–TiO^{2+} complexes.

Extended X-ray absorption fine structure (EXAFS) spectra at the V and Ti K-edges were fitted to further validate the local structure. V K-edge EXAFS fitting (Fig. S12 and Table S1, SI) showed that TiO^{2+} addition decreased the coordination number of the O1 shell at $R = 1.6$ Å and increased that of the O2 shell at $R = 2.0$ Å, consistent with heterocationic V–O–Ti bridge formation. The oxygen atoms of VO_2^+ as an electron donor coordinate to the electron-deficient Ti center in TiO^{2+}. In the Ti K-edge EXAFS spectra, the Ti–O distance increased after VO_2^+ was introduced into the TiO^{2+} solution (Fig. S13 and Table S2, SI). Wavelet-transform EXAFS provided additional bond-length information (Fig. 2g, h and S14, SI). These experimental trends agree with calculated bond lengths for VO_2^+, TiO^{2+}, and VO_2^+–TiO^{2+} structures (Fig. S15 and S16, SI), indicating changes in the local coordination environments of both VO_2^+ and TiO^{2+} upon mixing. Together with the results from MS, Raman spectroscopy, ^{51}V NMR and AIMD simulations, these observations collectively support the formation of VO_2^+–TiO^{2+} complexes through heterocationic V–O–Ti bridges.

To evaluate the stabilizing effect, 0.4 M TiO^{2+} was added to a 2 M V(v) electrolyte. The stability time increased from 12 h to 40 d at 50 °C (Fig. S17, SI), demonstrating that the formation of VO_2^+–TiO^{2+} motifs markedly improved both the V(v) concentration and high-temperature electrolyte stability. We then proceeded to clarify how TiO^{2+} alters V_2O_5 precipitation by Raman spectroscopy. A TiO^{2+}/H_2SO_4 control solution showed H_2SO_4 association and TiO^{2+} depolymerization with increasing temperature, as indicated by the disappearance of the 702 cm^{-1} band (Fig. S18, SI). In contrast, variable-temperature Raman spectra of the VO_2^+ electrolyte containing TiO^{2+} showed that the V–O–Ti bands at 476 and 757 cm^{-1} remained nearly unchanged (Fig. S19, SI), confirming the thermal persistence of VO_2^+–TiO^{2+} interactions. The slight blue shift of the 757 cm^{-1} band may be associated with disaggregation of VO_2^+–TiO^{2+} multimers. At 50 °C, no obvious spectral evolution was detected within the experimental time window (Fig. S20, SI). Therefore, to capture the precipitation pathway in the Ti-containing electrolyte, an accelerated *in situ* Raman experiment was conducted at 80 °C (Fig. 2i). The process can be divided into three stages (Fig. 2j). First, the 809 cm^{-1} band assigned to blue-shifted V–O–Ti bridge vibration disappeared, indicating V–O–Ti bond cleavage. Second, a band near 787 cm^{-1} appeared and continuously red-shifted, consistent with progressive V(v) condensation through V–O–V bonds. Finally, V_2O_5 Raman bands appeared, marking precipitation. Throughout the V–O–Ti to V–O–V conversion, the V–O vibration at around 480 cm^{-1} changed only slightly, suggesting limited alteration of the terminal V–O bond. These results demonstrate that TiO^{2+} delays V(v) condensation because heterocationic V–O–Ti bridges must first be broken before V–O–V bonds can form. At or below 50 °C, this bond-breaking step proceeds slowly and therefore effectively suppresses precipitation. TiO^{2+} acted as a molecular gatekeeper that captures oxo sites of VO_2^+ through V–O–Ti bridges, and thereby blocked the formation of V–O–V bonds and closed the condensation pathway of V(v) species.

We further observed concentration-dependent changes in the V–O–Ti bridge vibration. When the VO_2^+ concentration was 1.5 M, the V–O–Ti band initially appeared at 804 cm^{-1}. As TiO^{2+} concentration increased to 0.6 M, another band at 742 cm^{-1} emerged and became dominant (Fig. S21, SI). These multiple bands suggest the coexistence of several VO_2^+–TiO^{2+} motifs. To examine this effect, the TiO^{2+} concentration was fixed, while VO_2^+ concentration was varied. As shown in Fig. S22, SI, increasing VO_2^+ concentration shifted the dominant V–O–Ti band toward higher wavenumbers, opposite to the trend observed when TiO^{2+} concentration was increased. This behavior suggests that VO_2^+–TiO^{2+} motifs such as V–O(V)–Ti and V–O(Ti)–Ti units, as well as trimers or higher oligomers containing both VO_2^+ and TiO^{2+}, coexist in solution.[22,23] Changing the VO_2^+/TiO^{2+} ratio alters the aggregation extent and relative population of these motifs, leading to shifts in the bridge-vibration bands. The V–O–Ti band intensity also increased with H^+ concentration (Fig. S23, SI), implying that protons participate in deoxygenation steps during VO_2^+–TiO^{2+} coordination.[16] Overall, these results suggest that multiple VO_2^+–TiO^{2+} motifs, together with proton-involved deoxygenation, further stabilize cation–VO_2^+ oxygen-bridged coordination and contribute to the improved thermal stability of the electrolyte.

Stable VFB operation at elevated temperature

The electrochemical performance of Ti-containing vanadium electrolyte was evaluated by cyclic voltammetry (CV; Fig. 3a and b). Compared with the pristine electrolyte, TiO^{2+} addition increased the peak currents of both positive and negative redox reactions and decreased the separation between oxidation and reduction peaks for the negative half-cell, indicating improved reaction activity and enhanced reversibility of the V^{2+}/V^{3+} couple. For the negative electrolyte (Fig. S24, SI), the TiO^{2+}/Ti^{3+} redox couple exhibited a potential difference of 530 mV relative to the V^{2+}/V^{3+} redox couple. In a practical VFB, the side reaction can be avoided by increasing the discharge cut-off voltage (Fig. S25, SI). Therefore, except for the initial conversion of Ti(IV) to Ti(III) on the negative side during the first charging process, Ti did not participate in the electrochemical reactions during subsequent cycling. Electrochemical impedance spectroscopy (EIS) was then used to evaluate the interfacial charge-transfer behavior. The charge-transfer resistance R_{CT} decreased for both the VO^{2+}/VO_2^+ positive reaction and the V^{2+}/V^{3+} negative

© 2026 The Author(s). Published by the Royal Society of Chemistry

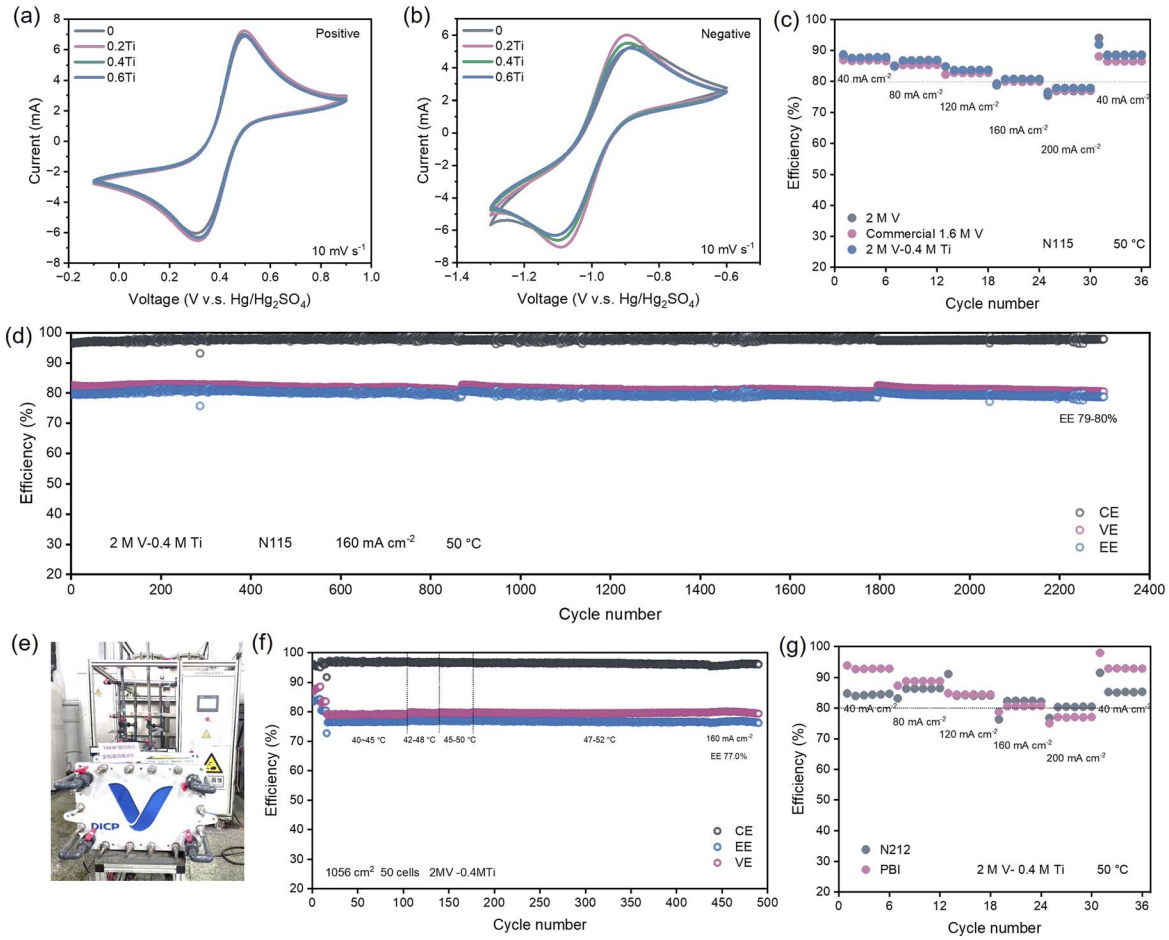


Fig. 3 Performance of a VFB assembled with an electrolyte with TiO^{2+}. Cyclic voltammetry of (a) diluted 2 M VO^{2+}/VO_2^+ electrolyte containing various TiO^{2+} concentrations at 10 mV s^{-1} and (b) diluted 2 M V^{2+}/V^{3+} electrolyte containing various Ti^{3+} concentrations at 10 mV s^{-1}. (c) Rate performance of VFBs using 2 M V-0.4 M Ti, 2 M V and commercial 1.6 M V electrolyte at 50 °C. (d) Cycle performance of VFBs with 2 M V-0.4 M Ti electrolyte at 160 mA cm^{-2} and a temperature of 50 °C. (e) Photo of a VFB stack, which consisted of 50 single cells connected in series with an area of 1056 cm^2. (f) Cycle performance of a VFB stack assembled with 2 M V-0.4 M Ti electrolyte with starting operating temperature of the thermal management system set as 52 °C. (g) Rate performance of a VFB assembled with Nafion 212 and PBI membranes at 50 °C; the 2 M V–0.4 M Ti electrolyte was used.

reaction after Ti addition (Fig. S26, Tables S3 and S4, SI). These results indicate that adding TiO^{2+} as the stabilizer can facilitate interfacial charge transfer as well.

Single cells (48 cm^2, with Nafion 115 membrane) using 2 M V electrolyte with 0.4 M TiO^{2+} in both positive and negative tanks were tested for rate performance at room temperature (Fig. S27, SI) and at 50 °C (Fig. 3c). The Ti-containing electrolyte showed no loss of energy efficiency (EE) relative to commercial 1.6 M V electrolyte or pristine 2 M V electrolyte. At 50 °C, it delivered particularly strong performance, with an EE of 80.7% at 160 mA cm^{-2} (Table S5, SI). Long-term cycling was then conducted at 160 mA cm^{-2} and 50 °C. A cell using commercial electrolyte showed severe capacity decay within fewer than 100 cycles (Fig. S28, SI). In contrast, the Ti-containing electrolyte enabled stable cycling without abrupt capacity loss (Fig. S29, SI). The cell cycled for more than 2000 cycles with an average EE of approximately 80% (Fig. 3d), and the corresponding charge/discharge curves are shown in Fig. S30, SI. During cycling, the electrolyte was regenerated twice to rebalance capacity loss caused by crossover (see Note S1, SI, for details of electrolyte regeneration). After cycling, the positive carbon felt from the Ti-containing and commercial-electrolyte cells was collected. The carbon felt from the commercial-electrolyte cell was covered with reddish-brown solids, explaining the rapid capacity decay (Fig. S31, SI), whereas no visible solids were observed on the carbon felt from the Ti-containing electrolyte cell. SEM images further confirmed the absence of V_2O_5 deposits in the Ti-containing electrolyte cell and the presence of abundant V_2O_5 particles in the commercial-electrolyte cell (Fig. S32, SI). These observations confirm that TiO^{2+} addition enhances electrolyte thermal stability and enables long-term VFB operation at elevated temperature.

Encouraged by the single-cell results, we assembled a 10 kW VFB stack with an active area of 1056 cm^2 per cell (Fig. 3e) to assess the practical scalability of the 2 M V electrolyte containing TiO^{2+}. The stack delivered a rated power of 10 kW and used

© 2026 The Author(s). Published by the Royal Society of Chemistry

100 L electrolyte on each side. Because of the improved thermal stability, the thermal-management start temperature could be set to 52 °C (Fig. S33(a), SI), higher than the operating temperature typically required for commercial electrolyte, which is generally below 45 °C as reported previously.[26,27] The higher set point is expected to reduce thermal-management energy consumption. The stack operated for approximately 500 cycles with a cumulative cycling time approaching 400 h and an energy efficiency of 77% at 160 mA cm^{-2} (Fig. 3f). No electrolyte rebalancing or regeneration was performed throughout stack operation. The operating temperature fluctuated between 47 and 52 °C (Fig. S33(a), SI). The data of discharge capacity and flow rate are displayed in Fig. S33(b) and (c), SI. This successful stack demonstration confirms the role of TiO^{2+} in extending electrolyte thermal stability and supports the further scale-up of high-temperature VFB operation. To further verify the compatibility of Ti-containing electrolyte with different membranes, single cells assembled with Nafion 212 and polybenzimidazole (PBI) membranes were also tested (Fig. 3g and S34, SI). At 50 °C, the Nafion 212-based cell delivered a remarkable energy efficiency of 80.4% at a current density of 200 mA cm^{-2}, while the PBI-based cell also achieved a high energy efficiency of 80.6% at 160 mA cm^{-2}.

Economic analysis of a system with Ti-containing electrolyte

To further evaluate the practical feasibility of Ti-containing electrolyte, a cost analysis was conducted for VFB systems using Ti-containing and commercial electrolytes (Fig. 4). Ti-containing electrolyte consisted of 2 M V and 0.4 M Ti. Due to higher vanadium concentration and the addition of Ti salt, the volumetric electrolyte cost increased to \$ 4680 m^{-3}, compared with \$ 3550 m^{-3} for the commercial electrolyte. The enhanced thermal stability of the Ti-containing electrolyte enabled the catholyte to remain stable for 40 days at 50 °C and SOC above 95%. Accordingly, the VFB using Ti-containing electrolyte could operate at a higher electrolyte utilization of 95%. Moreover, when operated at elevated temperature, the VFB achieved an energy efficiency of up to 81% (referred EE at 160 mA cm^{-2}). As a result of the increased electrolyte utilization, the electrolyte volume required per kWh decreased from 22 to 16 L.

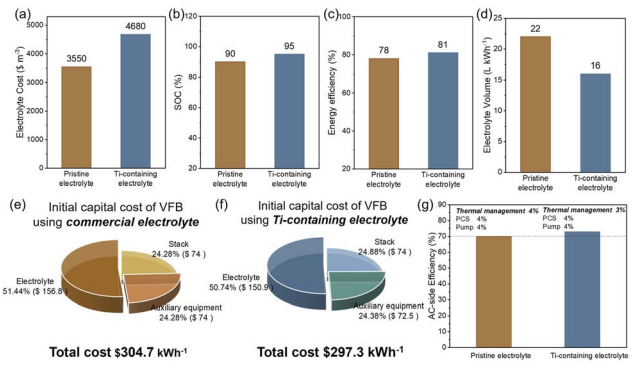


Fig. 4 Economic analysis of Ti-containing electrolyte. (a) Volumetric electrolyte cost of Ti-containing electrolyte and commercial electrolyte. (b) SOC and (c) energy efficiency of a VFB using Ti-containing electrolyte and commercial electrolyte. (d) Electrolyte volume required per kWh, (e and f) initial capital cost and (g) AC-side efficiency of the VFB system using Ti-containing electrolyte and commercial electrolyte.

The total life-cycle cost consists of initial capital cost and cumulative operating cost. Considering these factors discussed above, the initial capital cost of the VFB system decreases by \$7.4 per kWh (Fig. 4e and f) compared with that of the system using the commercial electrolyte. This reduction resulted from the reduction in electrolyte cost per unit energy and auxiliary equipment cost. During operation, the higher temperature threshold for activating the thermal-management system reduced thermal-management energy consumption from 4% to 3%, thereby reducing the operating cost. Consequently, the AC-side efficiency was increased to 73% (*vs.* 70% for commercial electrolyte shown in in Fig. 4g). These results demonstrate that the Ti-containing electrolyte provides a clear economic advantage at the system level.

Universality of the heterocationic coordination-gating strategy

TiO^{2+} enabled stable high-temperature VFB operation by forming heterocationic V–O–Ti oxygen bridges with VO_2^+ and thereby inhibiting V–O–V condensation. The cationic oxygen-bridged coordination enhanced the electrolyte stability. To determine whether this heterocationic coordination-gating strategy is general, we examined the interactions between VO_2^+ and a series of common cations. Additives were selected from the third period (Mg^{2+} and Al^{3+}) and the first transition-metal series (TiO^{2+}, VO^{2+}, Cr^{3+}, Mn^{2+}, Fe^{3+}, Co^{2+}, Ni^{2+}, Cu^{2+}, and Zn^{2+}). Raman spectroscopy was used to identify VO_2^+–cation interactions. In principle, V–O–M vibrations should appear in the ranges of 700–900 and 450–500 cm^{-1}, based on prior reports.[14–16] As shown in Fig. 5a and S35, SI, new V–O–M bands were observed after adding TiO^{2+}, VO^{2+}, Cr^{3+} or Fe^{3+} to V(v) electrolyte, indicating that VO_2^+ can coordinate with these cations. AIMD simulations (Fig. 5b) and variable-temperature Raman spectroscopy (Fig. S36, SI) further confirmed the stability of VO_2^+–VO^{2+}, VO_2^+–Cr^{3+}, and VO_2^+–Fe^{3+} heterocationic motifs; the VO_2^+–TiO^{2+} motifs were validated above (Fig. 2d, e and S15, SI). Thermal-stability tests of V(v) electrolytes with different cation additives (Fig. 5c and S37, SI) showed that cations capable of forming V–O–M bridges with VO_2^+ (TiO^{2+}, VO^{2+}, Cr^{3+} and Fe^{3+}) provided longer stability times. Among them, TiO^{2+} and Cr^{3+} stabilized 2 M V(v) electrolyte at 50 °C for more than 10 days. These results confirm that VO_2^+–cation oxygen-bridged coordination governs their coordination-gating efficacy, which shuts down V–O–V condensation and improves thermal stability of electrolytes. This coordination-gating capability can serve as a screening criterion for additives in high-temperature-stable electrolytes.

^{51}V NMR spectra (Fig. 5d) showed cation-dependent chemical-shift changes, indicating that TiO^{2+}, VO^{2+}, Cr^{3+} and Fe^{3+} modify the VO_2^+ solvation environment. Viscosity and conductivity measurements further differentiated these additives (Fig. 5e and f). Although the Ti-containing electrolyte did not show the lowest viscosity, it retained relatively high

© 2026 The Author(s). Published by the Royal Society of Chemistry

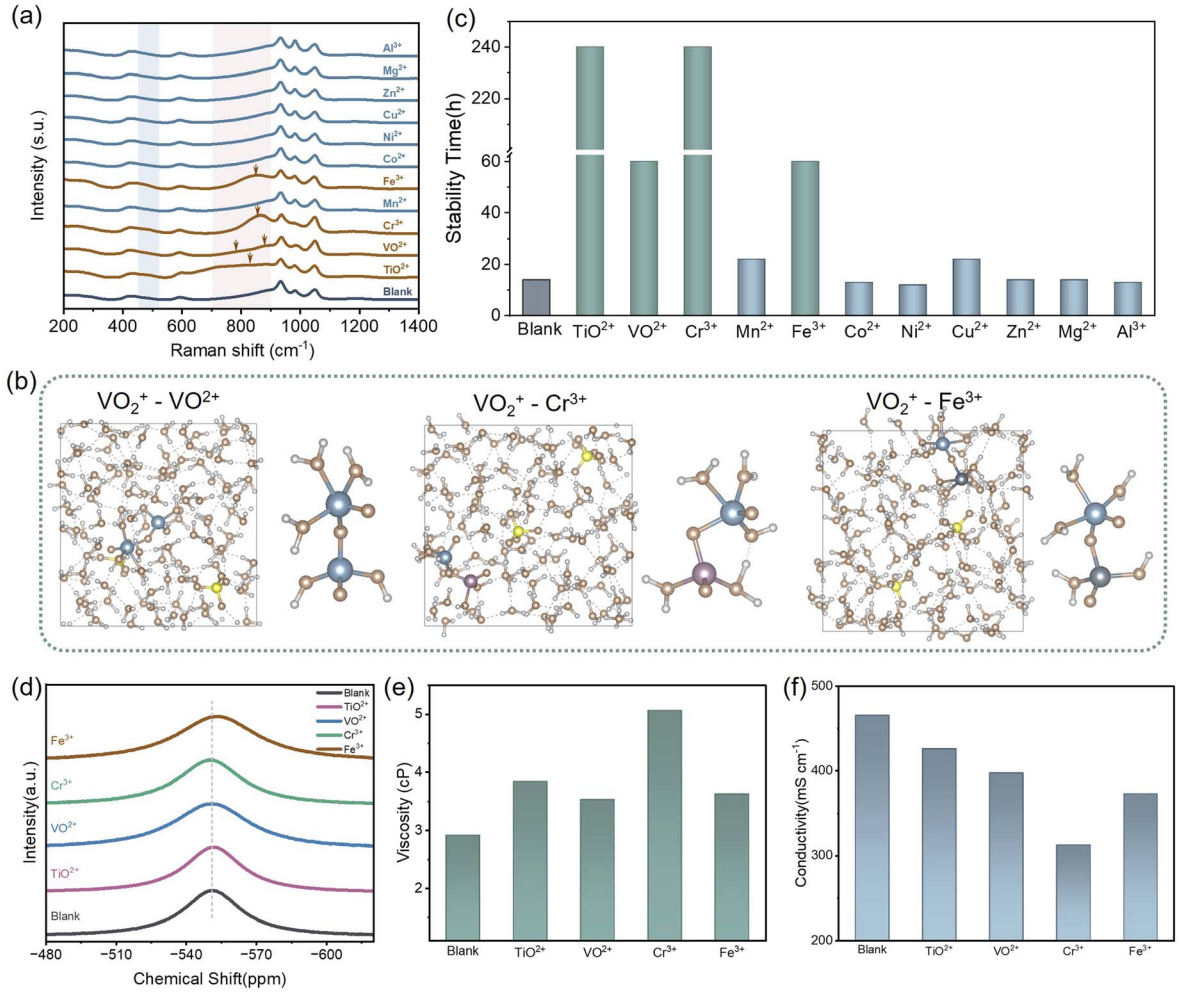


Fig. 5 Universality of the heterocationic coordination-gating strategy. (a) Raman spectra of 1.5 M VO_2^+ electrolytes with different cation additives; the cation concentration is 0.4 M. (b) Representative AIMD configurations of VO_2^+ with different cations (VO^{2+}, Cr^{3+} and Fe^{3+}), showing local coordination structures at 298 K. (c) Stability times of 2 M VO_2^+ electrolytes with different cation additives at 50 °C. (d) ^{51}V NMR spectra of 1.5 M VO_2^+ electrolytes with or without 20 mM cation additives (TiO^{2+}, VO^{2+}, Cr^{3+} and Fe^{3+}). (e) Viscosity and (f) conductivity of 1.5 M VO_2^+ electrolytes with different cation additives (TiO^{2+}, VO^{2+}, Cr^{3+} and Fe^{3+}); the cation concentration is 0.4 M.

conductivity compared with the other cation-containing electrolytes. Because high conductivity is favorable for electrolyte electrochemical performance, TiO^{2+} represents a practical additive for improving long-term VFB operation. These cationic interactions are not limited to VO_2^+–cation combinations. To further examine heterocationic oxygen-bridged coordination, pairwise mixtures of TiO^{2+}, VO^{2+}, Cr^{3+} and Fe^{3+} were prepared in 3 M H_2SO_4, and their Raman spectra were collected (Fig. S38, SI). TiO^{2+} formed Ti–O–M bridges with VO^{2+}, Cr^{3+} and Fe^{3+}, as indicated by new bands in the 800–900 cm^{-1} region. This result supports the proposed VO_2^+–TiO^{2+} motifs that include Ti-bridged units, such as V–O(Ti)–Ti. More broadly, heterocationic oxygen-bridged coordination provides a useful handle for regulating cation solvation structures beyond VO_2^+ itself.

Conclusions

In summary, *in situ* Raman spectroscopy revealed V–O–V bond formation as a critical step in the high-temperature precipitation of V(v) electrolyte. On this mechanistic basis, we designed a heterocationic coordination-gating strategy that suppresses V–O–V condensation through heterocationic V–O–M oxygen bridges. Ti(iv), present as TiO^{2+} in acidic electrolyte, was selected as an additive because it forms stable V–O–Ti bridges with VO_2^+. These bridges occupy heterocationic coordination nodes, block V–O–V formation, and gate the condensation pathway of V(v) species. As a result, the designed 2 M vanadium electrolyte remains stable for 40 days in the pentavalent state at 50 °C. VFBs using the Ti-containing electrolyte achieve long-term operation at elevated temperature, cycling for more than 2000 cycles at 50 °C without precipitation. A 10 kW stack further operated for nearly 500 cycles, while allowing the thermal-management system set point to be raised to 52 °C. Moreover, Ti-containing electrolyte reduces the system cost and increases AC-side efficiency, demonstrating the economic feasibility at the system level. In addition, interactions between VO_2^+ and selected cations were shown to be general, providing a practical screening criterion for high-temperature electrolyte additives.

© 2026 The Author(s). Published by the Royal Society of Chemistry

Overall, this work establishes cation–VO_2^+ coordination interaction regulation as a mechanistically grounded strategy for designing thermally stable vanadium electrolytes for large-scale VFB applications.

Author contributions

H. L. performed the experiments, analysed the data, and wrote the initial draft of the manuscript. Z. Z. and S.C. designed the calculation methods and oversaw the results. F. X. and T. L. conducted stack measurements. J. J and L. H designed and conducted the TOF-MS experiment. C. X. and X. L. designed and oversaw the experiments, and revised and finalized the manuscript for submission. All authors reviewed the manuscript.

Conflicts of interest

There are no conflicts to declare.

Data availability

The data supporting this article have been included as part of the supplementary information (SI). Ref. 28–43 are cited in the SI. Supplementary information: materials, methods, Fig. S1–S38, Note S1, and Tables S1–S5. See DOI: https://doi.org/10.1039/d6sc07112k.

Acknowledgements

This work was financially supported by the National Natural Science Foundation of China (Grant No. 22525081 and 22478379), Science and Technology Major Project of Liaoning Province (Grant No. 2024JH1/11700011), Liaoning Binhai Laboratory (No. LBLD-2024-01), commanding heights of science and technology of Chinese Academy of Sciences (Grant No. LDES15 0000), CAS Strategic Leading Science & Technology Program (A) (XDA0400201), and Liaoning Bidding for Key Technology Project (2023JH1/11200015 and 2023JH1/10400065). We also gratefully appreciate the Wuhan Supercomputing Center and the Supercomputing Center of Wuhan University for the generous computing resources to support our research efforts.

References

1 B. Dunn, H. Kamath and J. M. Tarascon, *Science*, 2011, **334**, 928–935.
2 T. Jiang, D. Shen and Z. Zhang, *Nat. Rev. Clean Technol.*, 2025, **1**, 474–492.
3 M. Vijayakumar, L. Li and G. Graff, *J. Power Sources*, 2011, **196**, 3669–3672.
4 N. V. Roznyatovskaya, V. A. Roznyatovsky and C.-C. Höhne, *J. Power Sources*, 2017, **363**, 234–243.
5 V. Murugesan, Z. Nie and X. Zhang, *Cell Rep. Phys. Sci.*, 2021, **2**, 100323.
6 T. D. Nguyen, A. Whitehead and N. Wai, *Small*, 2024, **20**, 2311771.
7 C. Mu, T. Li and C. Zhan, *Angew. Chem., Int. Ed.*, 2025, **64**, e202508456.
8 H. Long, C. Liao and C. Xie, *J. Energy Chem.*, 2025, **106**, 1038–1045.
9 C. Mu, C. Zhan and T. Li, *Chem. Sci.*, 2026, **17**, 11403–11411.
10 M. L. McKee and M. Swart, *Inorg. Chem.*, 2005, **44**, 6975–6982.
11 J. C. Sullivan, J. C. Hindman and A. J. Zielen, *J. Am. Chem. Soc.*, 1961, **83**, 3373–3378.
12 T. A. Sullens, R. A. Jensen and T. Y. Shvareva, *J. Am. Chem. Soc.*, 2004, **126**, 2676–2677.
13 S. Skanthakumar, M. R. Antonio and L. Soderholm, *Inorg. Chem.*, 2008, **47**, 4591–4595.
14 R. K. Murmann and J. C. Sullivan, *Inorg. Chem.*, 1967, **6**, 892–900.
15 C. Madic, G. M. Begun and D. E. Hobart, *Radiochim. Acta*, 1983, **34**, 195–202.
16 C. Madic, G. M. Begun and R. L. Hahn, *Inorg. Chem.*, 1984, **23**, 469–476.
17 J. Beukenkamp and K. D. Herrington, *J. Am. Chem. Soc.*, 1960, **82**, 3025–3031.
18 K. Tomikawa and H. Kanno, *J. Phys. Chem. A*, 1998, **102**, 6082–6088.
19 D. A. Knopf, B. P. Luo and U. K. Krieger, *J. Phys. Chem. A*, 2003, **107**, 4322–4332.
20 S. Lee, *Solid State Ionics*, 2003, **165**, 111–116.
21 N. Kausar, R. Howe and M. Skyllas-Kazacos, *J. Appl. Electrochem.*, 2001, **31**, 1327–1332.
22 P. Comba and A. Merbach, *Inorg. Chem.*, 1987, **26**, 1315–1323.
23 Y.-R. Dong, H. Kaku and K. Hanafusa, *ECS Trans.*, 2015, **69**, 59–67.
24 C. Choi, S. Kim and R. Kim, *Renewable Sustainable Energy Rev.*, 2017, **69**, 263–274.
25 F. Tian, L. Wang and C.-S. Wang, *J. Energy Chem.*, 2018, **27**, 1376–1380.
26 C. Hu, Y. Dong and W. Zhang, *Electrochim. Acta*, 2023, **462**, 142762.
27 W. Tian, H. Du and J. Wang, *Materials*, 2023, **16**, 4582.
28 B. Ravel and M. Newville, *J. Synchrotron Radiat.*, 2005, **12**, 537–541.
29 S. I. Zabinsky, J. J. Rehr and A. Ankudinov, *Phys. Rev. B: Condens. Matter Mater. Phys.*, 1995, **52**, 2995–3009.
30 G. Kresse and J. Furthmüller, *Comput. Mater. Sci.*, 1996, **6**, 15–50.
31 G. Kresse and J. Furthmüller, *Phys. Rev. B: Condens. Matter Mater. Phys.*, 1996, **54**, 11169–11186.
32 J. P. Perdew, K. Burke and M. Ernzerhof, *Phys. Rev. Lett.*, 1996, **77**, 3865–3868.
33 P. E. Blöchl, *Phys. Rev. B: Condens. Matter Mater. Phys.*, 1994, **50**, 17953–17979.
34 G. Kresse and D. Joubert, *Phys. Rev. B: Condens. Matter Mater. Phys.*, 1999, **59**, 1758–1775.
35 W. G. Hoover, *Phys. Rev. A: At., Mol., Opt. Phys.*, 1985, **31**, 1695–1697.
36 S. Nosé, *J. Chem. Phys.*, 1984, **81**, 511–519.

© 2026 The Author(s). Published by the Royal Society of Chemistry

37 S. Grimme, J. Antony and S. Ehrlich, *J. Chem. Phys.*, 2010, **132**, 154104.
38 M. J. Frisch, G. W. Trucks and H. B. Schlegel, *Gaussian 16 Rev. C.01*, Wallingford, CT, 2016.
39 A. D. Becke, *J. Chem. Phys.*, 1993, **98**, 5648–5652.
40 C. Lee, W. Yang and R. G. Parr, *Phys. Rev. B: Condens. Matter Mater. Phys.*, 1988, **37**, 785–789.
41 S. Grimme, S. Ehrlich and L. Goerigk, *J. Comput. Chem.*, 2011, **32**, 1456–1465.
42 A. V. Marenich, C. J. Cramer and D. G. Truhlar, *J. Phys. Chem. B*, 2009, **113**, 6378–6396.
43 K. Wolinski, J. F. Hinton and P. Pulay, *J. Am. Chem. Soc.*, 1990, **112**, 8251–8260.

© 2026 The Author(s). Published by the Royal Society of Chemistry